Degeneracies in Sky Localisation Determination from a Spinning Coalescing Binary through Gravitational Wave Observations: a Markov-Chain Monte-Carlo Analysis for two Detectors.

V. Raymond[1], M.V. van der Sluys[1], I. Mandel[1], V. Kalogera[1], C. Röver[2,3], N. Christensen[4]

[1] Dept. of Physics & Astronomy, Northwestern University, 2131 Tech Drive, Evanston IL, 60208, USA

[2] Department of Statistics, University of Auckland, Private Bag 92019, Auckland 1142, New Zealand

[3] Max-Planck-Institut für Gravitationsphysik, Callinstraße 38, 30167 Hannover, Germany

[4] Physics & Astronomy Dept., Carleton College, One North College Street, Northfield MN 55057, USA

E-mail: `vivien@u.northwestern.edu`

Abstract. Gravitational-wave signals from inspirals of binary compact objects (black holes and neutron stars) are primary targets of the ongoing searches by ground-based gravitational-wave interferometers (LIGO, Virgo, and GEO-600). We present parameter-estimation simulations for inspirals of black-hole–neutron-star binaries using Markov-chain Monte-Carlo methods. As a specific example of the power of these methods, we consider source localisation in the sky and analyse the degeneracy in it when data from only two detectors are used. We focus on the effect that the black-hole spin has on the localisation estimation. We also report on a comparative Markov-chain Monte-Carlo analysis with two different waveform families, at 1.5 and 3.5 post-Newtonian order.

1. Introduction

Binary systems with compact objects — neutron stars (NSs) and black holes (BHs) — in the mass range $\sim 1\,M_\odot - 100\,M_\odot$ are among the most likely sources of gravitational waves (GWs) for ground-based laser interferometers currently in operation (Cutler & Thorne 2002): LIGO (Barish & Weiss 1999), Virgo (Acernese et al. 2004) and GEO-600 (Willke et al. 2004). Merger-rate estimates are quite uncertain and for BH-NS binaries current detection-rate estimates range from 0.0003 to $0.1\,\mathrm{yr}^{-1}$ for first-generation instruments (*e.g.* O'Shaughnessy et al. 2008). Upgrades to Enhanced LIGO/Virgo (2008–2009) and Advanced LIGO/Virgo (2011–2014) are expected to increase detection rates by factors of about ~ 10 and $\sim 10^3$, respectively.

The measurement of source properties holds major promise for improving our astrophysical understanding and requires reliable methods for parameter estimation. This is a challenging problem, however, because of the large number of parameters (9 for circular non-spinning binaries, and more for spinning systems) and the significant amount of structure in the parameter space. In the case of low-mass-ratio binaries (*e.g.* BH-NS), these issues are amplified for significant spin magnitudes and large misalignments between the BH spin and the orbital angular momentum (Apostolatos et al. 1994, Grandclément et al. 2003, Buonanno et al. 2003). However, the presence of spins improves parameter estimation through the signal modulations, although still presenting us with a considerable computational challenge. This was highlighted in the context of LISA observations (see Vecchio 2004, Lang & Hughes 2006) and in our first study devoted to ground-based observations (van der Sluys et al. 2008b).

In this paper we examine the potential for parameter estimation of spinning binary inspirals with ground-based interferometers. Röver et al. (2006, 2007a) explored parameter estimation for non-spinning binaries, which requires 9 parameters. We focus on BH-NS binaries, which can exhibit significant coupling between the orbital angular momentum and the BH spin, mainly because of the high mass ratio (Apostolatos et al. 1994), while at the same time we are justified to ignore the NS spin, leading to a 12-dimensional parameter space. We apply a newly developed Markov-chain Monte-Carlo (MCMC) algorithm (van der Sluys et al. 2008a) to spinning inspiral signals injected into synthetic noise and we derive posterior probability-density functions (PDFs) of all twelve signal parameters. In our previous study (van der Sluys et al. 2008b), we showed the accuracy obtained in sky-position determination using data from a two-detector network, where a degeneracy in the sky position exists, and from a three-detector network, where the degeneracy is broken. Following this work, we here analyze in further detail the degeneracy which is present when data from only two detectors are used. In section 4.2 we show that the degeneracy in the sky position is reduced but not lifted when a significant spin is present ($a_{\mathrm{spin}} \geq 0.5$), and that a sufficient angle between spin and orbital angular momentum can break such a degeneracy ($\theta_{SL} \geq 55°$). In this study, we demonstrate that these degeneracies are due to a high degree of similarity between signals from sources with significantly different parameter sets, while we made

sure the observed effects are real and not in fact artifacts due to potential errors in our analysis methodology.

In section 4.3, we also demonstrate that the inclusion of higher post-Newtonian orders in the waveform can improve the accuracy of intrinsic-parameter estimation. Meanwhile, we find that the additional structure in the parameter space of higher-order waveforms lowers the sampling efficiency of the MCMC and requires improvements to the sampling scheme.

2. Signal and observables

In this paper we analyze the signal produced during the inspiral phase of two compact objects of masses $M_{1,2}$ in circular orbit. We focus on a fiducial BH-NS binary system with $M_1 = 10\,M_\odot$ and $M_2 = 1.4\,M_\odot$, and we ignore the NS spin. The BH spin $\mathbf{S}$ couples to the orbital angular momentum $\mathbf{L}$, leading to amplitude and phase modulations of the observed gravitational radiation due to the precession of the orbital plane. Here we model GWs by post-Newtonian (pN) waveforms, either at 1.5-pN order in phase and Newtonian amplitude or at 3.5-pN order in phase and Newtonian amplitude. For the latter waveform we use the implementation from the LSC Algorithm Library (LAL) (LIGO Scientific Collaboration 2007). In our analysis we model the noise in each detector as a zero-mean Gaussian, stationary random process, with one-sided noise spectral density $S_a(f)$, at the initial-LIGO design sensitivity (Fritschel 2003).

2.1. Waveform template at the 1.5-pN order

We adopt the *simple-precession* limit (Eqs. 51, 52, 59 & 63 in Apostolatos et al. 1994), appropriate for the single-spin system considered here. For simplicity (to speed up the waveform calculation), we also ignore the *Thomas precession* (Apostolatos et al. 1994). In this approximation, the orbital angular momentum $\mathbf{L}$ and spin $\mathbf{S}$ precess with the *same* angular frequency around a fixed direction $\hat{\mathbf{J}}_0 \approx \hat{\mathbf{J}}$, where $\mathbf{J} = \mathbf{L} + \mathbf{S}$. During the inspiral phase the spin misalignment $\theta_{SL} \equiv \arccos(\hat{\mathbf{S}} \cdot \hat{\mathbf{L}})$ and $S = |\mathbf{S}|$ are constant. These approximate waveforms retain (at the leading order) all the prominent qualitative features introduced by the spins, while allowing us to rapidly compute the waveforms analytically. While this approach is justified for the exploration of GW astronomy and the development of parameter-estimation algorithms, more accurate waveforms (*e.g.* Kidder 1995, Will & Wiseman 1996, Faye et al. 2006, Blanchet et al. 2006) will be necessary for the analysis of real signals (see section 4.3).

A circular binary inspiral with one spinning compact object is described by a 12-dimensional parameter vector $\vec{\lambda}$. With respect to a fixed geocentric coordinate system our choice of independent parameters is:

$$\vec{\lambda} = \{\mathcal{M}, \eta, \text{R.A.}, \sin\text{Dec}, \sin\theta_{J_0}, \phi_{J_0}, \log d_\text{L}, a_\text{spin}, \cos\theta_{SL}, \phi_\text{c}, \alpha_\text{c}, t_\text{c}\}, \quad (1)$$

where $\mathcal{M} = \frac{(M_1 M_2)^{3/5}}{(M_1 + M_2)^{1/5}}$ and $\eta = \frac{M_1 M_2}{(M_1 + M_2)^2}$ are the chirp mass and symmetric mass ratio, respectively; R.A. (right ascension) and Dec (declination) identify the source position
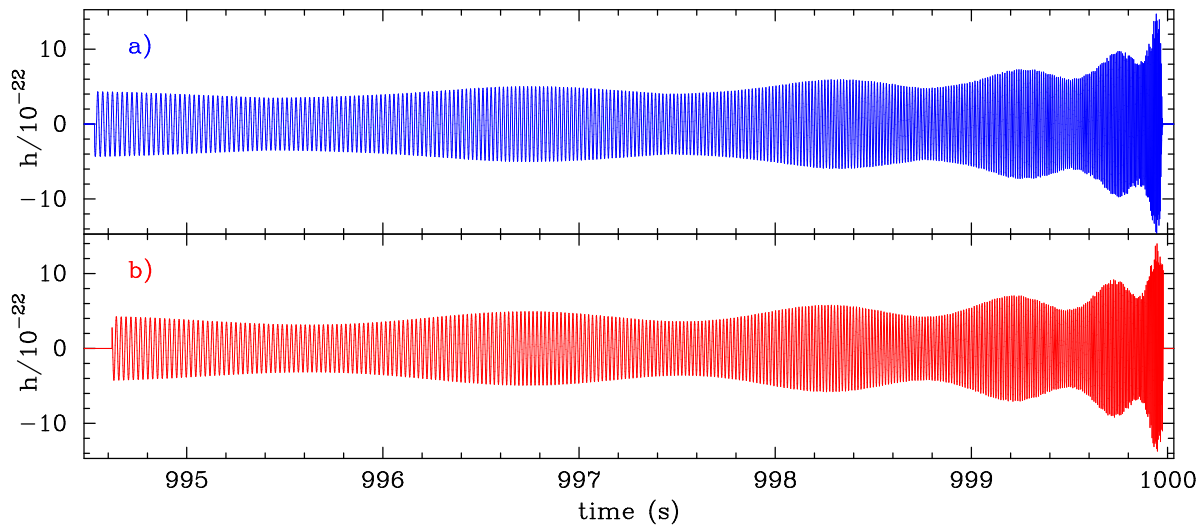
Figure 1. **(a)** Part of the 1.5-pN time-domain waveform from a source with $a_{\mathrm{spin}} = 0.5$ and $\theta_{SL} = 20°$. **(b)** The 3.5-pN waveform from a source with the same parameters. The waveforms start at $40\,\mathrm{Hz}$ and are aligned at the coalescence time.

in the sky; the angles $\theta_{J_0} \in \left[-\frac{\pi}{2}, \frac{\pi}{2}\right]$ and $\phi_{J_0} \in [0, 2\pi[$ identify the unit vector $\hat{\mathbf{J}}_0$; d_{L} is the luminosity distance to the source and $0 \leq a_{\mathrm{spin}} \equiv S/M_1^2 \leq 1$ is the dimensionless spin magnitude; ϕ_{c} and α_{c} are integration constants that specify the GW phase and the location of $\mathbf{S}$ on the precession cone, respectively, at the time of coalescence t_{c}, defined with respect to the center of the Earth.

Given a network comprising n_{det} detectors, the data collected at the $a-$th instrument ($a = 1, \ldots, n_{\mathrm{det}}$) is given by $x_a(t) = n_a(t) + h_a(t; \vec{\lambda})$, where $h_a(t; \vec{\lambda}) = F_{a,+}(t)\, h_{a,+}(t; \vec{\lambda}) + F_{a,\times}(t)\, h_{a,\times}(t; \vec{\lambda})$ is the GW strain at the detector (see Eqs. 2–5 in Apostolatos et al. 1994) and $n_a(t)$ is the detector noise. The astrophysical signal is given by the linear combination of the two independent polarisations $h_{a,+}(t; \vec{\lambda})$ and $h_{a,\times}(t; \vec{\lambda})$ weighted by the *time-dependent* antenna beam patterns $F_{a,+}(t)$ and $F_{a,\times}(t)$.

2.2. Waveform template in the 3.5-pN order

Although the 1.5-pN, simple-precession waveform is useful to investigate the principal effects of spin on parameter estimation, a more realistic waveform is needed to analyse detected signals. The waveform we use for this is 3.5-pN in phase and Newtonian amplitude. The implementation in the LSC Algorithm Library closely follows the first section of Buonanno et al. (2003). For comparison purposes we converted the usual set of parameters used in the LAL software to the parameters in Eq. 1. In doing so, we fix 3 of the 15 parameters of the LAL parameter set, setting the spin of the second member of the binary to be 0. The waveform is generated using `LALGenerateInspiral()` from the injection package (LIGO Scientific Collaboration 2007). An example of $h_a(t)$ for $a_{\mathrm{spin}} = 0.5$ and $\theta_{SL} = 20°$ for both waveforms is shown in figure 1.

3. Parameter estimation: Methods

The goal of our analysis is to determine the *posterior* probability density function (PDF) of the unknown parameter vector $\vec{\lambda}$ in Eq. 1, given the data sets x_a collected by a network of n_{det} detectors and the *prior* $p(\vec{\lambda})$ on the parameters. We use wide, flat priors (see van der Sluys et al. (2008a) for details). Bayes' theorem provides a rigorous mathematical rule to assign such a probability:

$$p(\vec{\lambda}|x_a) = \frac{p(\vec{\lambda})\,\mathcal{L}(x_a|\vec{\lambda})}{p(x_a)}\,; \tag{2}$$

in the previous equation

$$\mathcal{L}(x_a|\vec{\lambda}) \propto \exp\left(< x_a|h_a(\vec{\lambda}) > -\frac{1}{2} < h_a(\vec{\lambda})|h_a(\vec{\lambda}) >\right) \tag{3}$$

is the *likelihood function* of the data given the model, which measures the fit of the data to the model, and $p(x_a)$ is the *marginal likelihood* or *evidence*. We use the notation

$$< x|y >= 4Re\left(\int_{f_{\text{low}}}^{f_{\text{high}}} \frac{\tilde{x}(f)\tilde{y}^*(f)}{S_a(f)}\,\mathrm{d}f\right) \tag{4}$$

to denote the *overlap* of signals x and y, where $\tilde{x}(f)$ is the Fourier transform of $x(t)$. For future reference, we also define match between two waveforms corresponding to different parameter values as the overlap between the normalized waveforms:

$$M(h(\vec{\lambda_1}), h(\vec{\lambda_2})) = \frac{< h(\vec{\lambda_1})|h(\vec{\lambda_2}) >}{\sqrt{< h(\vec{\lambda_1})|h(\vec{\lambda_1}) >< h(\vec{\lambda_2})|h(\vec{\lambda_2}) >}} \tag{5}$$

Note that with the definitions employed here, the "true" likelihood computed at the parameters of the injected waveform $\mathcal{L}_{\text{true}}(x|\vec{\lambda}_{\text{true}})$ is a random variable that depends on a particular realization of the noise n_a in the data $x_a = h(\vec{\lambda}_{\text{true}}) + n_a$. We define the signal to noise ratio (SNR) to be the square root of twice the expectation value of $\log \mathcal{L}_{\text{true}}$:

$$SNR = \sqrt{< h(\vec{\lambda}_{\text{true}})|h(\vec{\lambda}_{\text{true}}) >} \tag{6}$$

For multi-detector observations involving a network of detectors with uncorrelated noise — this is the case of this paper, where we use up to two non-colocated detectors — we have $\mathcal{L}(\vec{x}|\vec{\lambda}) = \prod_{a=1}^{n_{\text{det}}} \mathcal{L}(x_a|\vec{\lambda})$, for $\vec{x} \equiv \{x_a : a = 1, \ldots, n_{\text{det}}\}$ and:

$$p(\vec{\lambda}|\vec{x}) = \frac{p(\vec{\lambda})\,\mathcal{L}(\vec{x}|\vec{\lambda})}{p(\vec{x})} \tag{7}$$

The numerical computation of the joint and *marginalised* PDFs involves the evaluation of integrals over a large number of dimensions. Markov-chain Monte-Carlo (MCMC) methods (*e.g.* Gilks et al. 1996, Gelman et al. 1997, and references therein) have proved to be especially effective in tackling these numerical problems. We developed an adaptive (see Figueiredo & Jain 2002, Atchadé & Rosenthal 2005) MCMC algorithm to explore the parameter space efficiently while requiring the least amount of tuning for the specific signal at hand; the code is an extension of the one developed by some of the authors to

explore MCMC methods for non-spinning binaries (Röver et al. 2006, Röver et al. 2007a) and takes advantage of techniques explored by some of us in the context of LISA data analysis (Stroeer et al. 2007). A summary of the methods used in our MCMC code was published in van der Sluys et al. (2008a); more technical details will be provided elsewhere.

4. Parameter estimation: Results

4.1. MCMC runs

Here we present results obtained by injecting a signal into simulated interferometer noise and computing the posterior PDFs with MCMC techniques, for a fiducial source consisting of a $10\,M_\odot$ spinning BH and a $1.4\,M_\odot$ non-spinning NS in a binary system at a distance of about $16\,\mathrm{Mpc}$ (see sections 4.2 and 4.3 for parameters values). We consider a number of cases for which we change the BH spin parameters. We run the analysis using the simulated data from (i) the 4-km LIGO detector at Hanford (H1) alone, (ii) the LIGO Hanford (H1) and a second detector with the initial-LIGO noise curve located and oriented in the same way as the Virgo detector near Pisa, which we denote by (P).

The MCMC analysis that we carry out on each data set consists of 5 to 25 independent chains, each with a length of several millions iterations. The chains are sampled after a *burn-in* period (see *e.g.* Gilks et al. 1996) that is determined automatically as follows: we determine the absolute maximum likelihood $\log(\mathcal{L}_{\mathrm{max}})$, defined as the highest likelihood $\log[\mathcal{L}(\vec{x}|\vec{\lambda})]$ obtained over the ensemble of parameters $\vec{\lambda}$ for which the overlap has been computed, for any of the individual chains. Then for each chain we include all the iterations *after* the chain reaches a likelihood value of $\log(\mathcal{L}_{\mathrm{max}}) - 2$ for the first time. All our Markov chains start at offset (*i.e.*, non-true) parameter values, unless specified otherwise. The starting values for $\mathcal{M}$ and t_{c} are drawn from a Gaussian distribution centred on the true parameter value, with a standard deviation of $0.1\,M_\odot$ and $30\,\mathrm{ms}$ respectively. The other ten parameters are drawn uniformly from the allowed ranges. Our MCMC code needs to run for typically a few days to one week in order to show the first results and 10–14 days to accumulate a sufficient number of iterations for good statistics, each chain using a single $2.8\,\mathrm{GHz}$ CPU.

4.2. A Ring in the Sky

For the study in this section, we use the 1.5-pN waveform with the *simple-precession* prescription only (see section 2.1). In order to further speed up the MCMC runs, we fixed the mass and spin parameters to the true parameter values, and performed test calculations to verify that this does not affect our conclusions.

As reference MCMC runs (experiment 1, see table 1), we injected signals into two simulated detectors (H1 and P). We made three different injections, which differed

Table 1. List of the experiments described in section 4.2. The sky ring is defined as the ring produced by experiment 1, composed of arcs and gaps.

experiment	injection position (in the sky ring)	sky position parameters	starting values (in the sky ring)
1	arc	free	offset (non true values)
2a	arc	fixed	true position (arc)
2b	arc	fixed	gap position (⭕)
3	gap (⭕)	free	offset (non true values)

in the spin magnitude values ($a_{\text{spin}} = 0.0, 0.5$) and the spin-misalignment values ($\theta_{SL} = 20°, 55°$) for $a_{\text{spin}} = 0.5$ case; the remaining parameters were kept constant across all three injections: $\mathcal{M} = 3.0 M_\odot$, $\eta = 0.11$ ($M_1 = 10.0 M_\odot$, $M_2 = 1.4 M_\odot$), $d_{\text{L}} = 16\,\text{Mpc}$, R.A. $= 14.3\,\text{h}$, Dec $= 11.5°$, $\theta_{J_0} = 3.8°$, $\phi_{J_0} = 289°$, $\phi_{\text{c}} = 305°$, $\alpha_{\text{c}} = 4°$ and $t_{\text{c}} = 700009012.345\,\text{s}$ GPS time.

For a detection with two interferometers, the sky position is degenerate; when no spin is present in the source, our PDFs show an incomplete sky ring where the source might be — long arcs separated by empty "gaps" — rather than one tightly constrained ring. When the BH is spinning, and especially when the misalignment angle between orbital angular momentum and spin is significant, the sky location constraint shrinks appreciably until much smaller arcs — or even a single arc — are left (see figure 2a).

In order to probe the nature of the gaps in the sky ring, we devised a second experiment (experiment 2, see table 1). For each run, we injected the same signal as before, but now forced the MCMC code to search for the other parameters while keeping the sky position fixed to either the true values (experiment 2a), or to the sky position in the gap that is labelled by the circle in the first panel of figure 2a (experiment 2b). Running the MCMC code in this way provides us with the combination of the free parameters that fits the data best, given the constraint in sky position (the *conditional* posterior distribution, conditional on the corresponding sky position). In particular, the code provides us with the highest likelihood that can be obtained for this sky position. These likelihoods are listed in table 2. They show that the maximum likelihood found in the gap is very similar to the likelihood of the injection for the non-spinning signal, whereas it is significantly lower in the case of the spinning signal. For the non-spinning signal, an unfavourable binary orientation (inclination $= 92.0°$) and hence a short distance ($d_{\text{L}} = 3.6\,\text{Mpc}$) are needed to give a good match for the given sky position. The modulations of the signal due to the precession of the binary orbit prevent this match in the spinning cases.

Thus, for a source with a non-spinning BH, a high likelihood *can* be found in the gaps of the sky ring. Therefore the absence of high likelihood values does *not* explain the fact that our Markov chains hardly sample this part of the parameter space. Instead, we find that the PDFs for some of the other parameters (especially the distance d_{L} and binary orientation $\arccos(\mathbf{J} \cdot \mathbf{N})$) are very narrow for experiment 2b compared to those

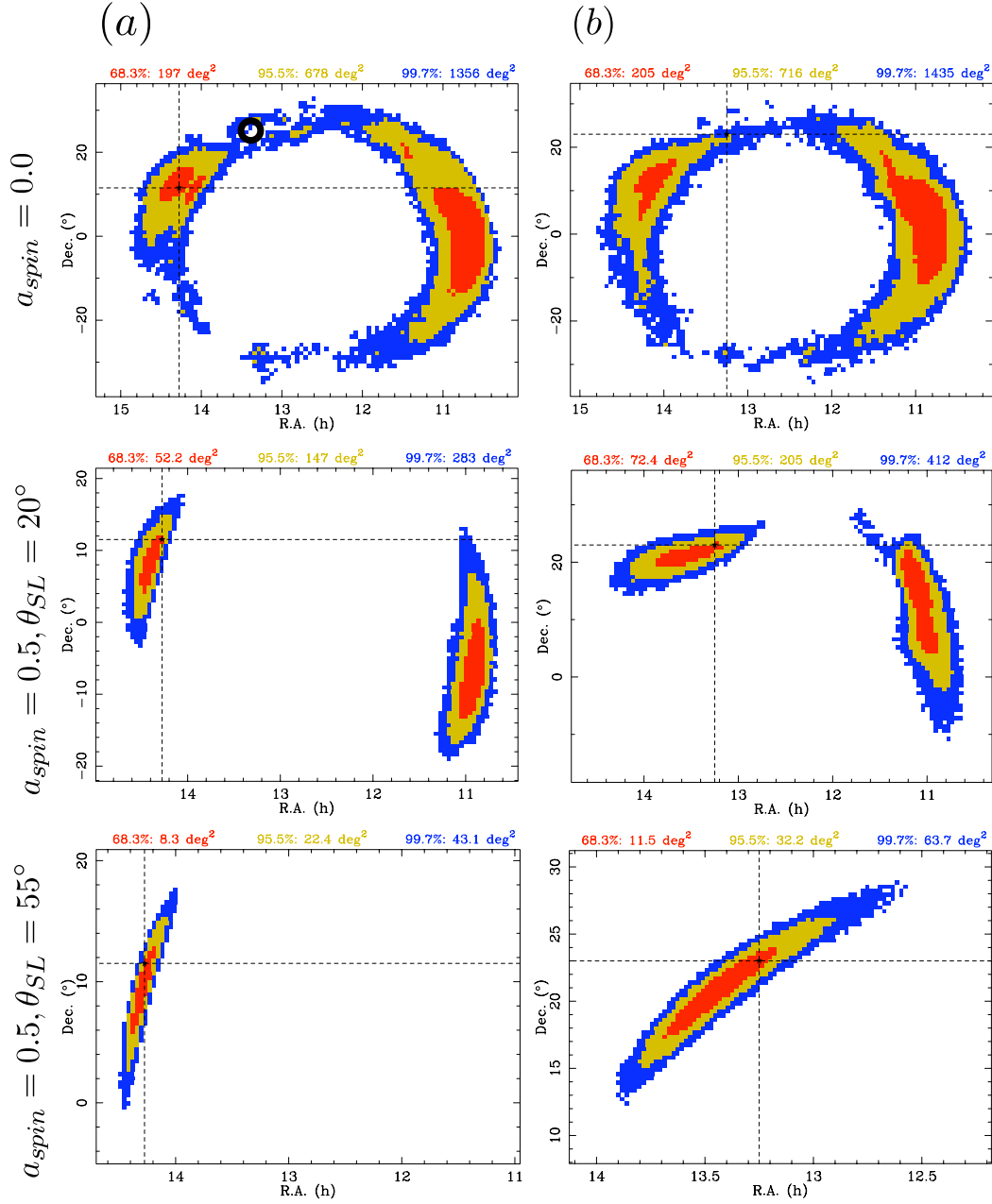**Figure 2.** Two-dimensional PDFs of the sky position for the MCMC runs as labelled. The colours show the different probability intervals (1-σ, 2-σ and 3-σ for red, yellow and blue respectively). The black dashed lines mark the position in the sky of the injection for each run. Left column **(a)**: results for the reference runs, experiment 1 (signal injection at R.A. = 14.3 h, Dec = 11.5°). The symbol O denotes the "gap" discussed in the text. Right column **(b)**: results for experiment 3: an MCMC run with a signal injection at O (R.A. = 13.25 h, Dec = 23°). For the non-spinning case, the PDFs are very similar to those in the original run, whereas they are very different for the spinning cases (notice the difference in the axis ranges).

Table 2. Likelihoods values recovered by the MCMC runs of experiment 2b for the sky ring, described in section 4.2.

	$a_{\text{spin}} = 0.0$	$a_{\text{spin}} = 0.5,$ $\theta_{SL} = 20°$	$a_{\text{spin}} = 0.5,$ $\theta_{SL} = 55°$	
network SNR	17.0	18.3	18.4	
$\log(\mathcal{L}(x_a|\vec{\lambda}_{\text{true}}))$	131	154	208	
$\log(\mathcal{L}_{\text{max}})$(O)	131	125	152	
Match $M(h(\vec{\lambda}_{\text{true}}), h(\vec{\lambda}_{\mathcal{L}_{\text{max}}}))$	99.5%	89.6%	82.5%	(between waveforms injected
(equation 5)				in experiment 1 and
				those corresponding to $\mathcal{L}_{\text{max}}$)
				(reference parameters,
$\mathcal{L}_{\text{max}}$ parameters :				injected in experiment 1)
position (R.A. [h], Dec. [°])	13.25, 23	13.25, 23	13.25, 23	14.3, 11.5
orientation (θ_{J_0} [°], ϕ_{J_0} [°])	-65.4, 10.8	-59.5, 340.4	-21.8, 169.5	3.8, 289
inclination ($\arccos(\mathbf{J} \cdot \mathbf{N})$) [°]	92.0	97.5	129.7	128.4
distance [Mpc]	3.7	11.1	18.3	16
$t_c - 700009010$ [s]	2.34955	2.34959	2.34960	2.34500

for experiment 2a (figure 3). This indicates that the overall volume of parameter space in these parameters is very small for sky positions in the gap and this is the reason that these gaps are not visited frequently by the chains. On a side note, our priors are flat and can not be the cause for this effect. If our MCMC runs had infinite length, they would sample this region in parameter space and bridge the gaps in figure 2a with a thin line, *i.e.* the points "bridging" the gaps will form a set of very small measure. Even with a perfect sampling, the same behavior is to be expected: the chains would mainly sample the arcs and rarely the gaps. Interestingly, the similarity in likelihood values between the true position and the gap for the case of a non-spinning BH also means that these two signals are virtually indistinguishable, *i.e.* their match (equation 5) is very high (99.5% see table 2). This indicates that if the source *were* truly in the gap, Markov chains of this length would not recover it, and chains of any length would not have a significant PDF in the gaps.

To illustrate this, we did a third experiment (experiment 3, see table 1). We injected a signal at the position in the gap labelled by O in figure 2a. We kept the same masses and spin values as before, and set the other parameters to the values yielding the maximum likelihoods from the second experiment, listed in table 2.

In the non-spinning case, the sky ring that is recovered is very similar to that of the original run (see figure 2b); the small difference seen can be explained by the fact that the match between the signal injected in experiment 3 and the signal injected in experiment 1 was 99.5%, not 100% (table 2). This shows that there exist carefully selected combinations of sky position, binary orientation and distance which cannot be easily recovered by our analysis. However, this reflects a *real* phenomenon; it is very improbable for a source to have the right orientation to produce the gravitational-
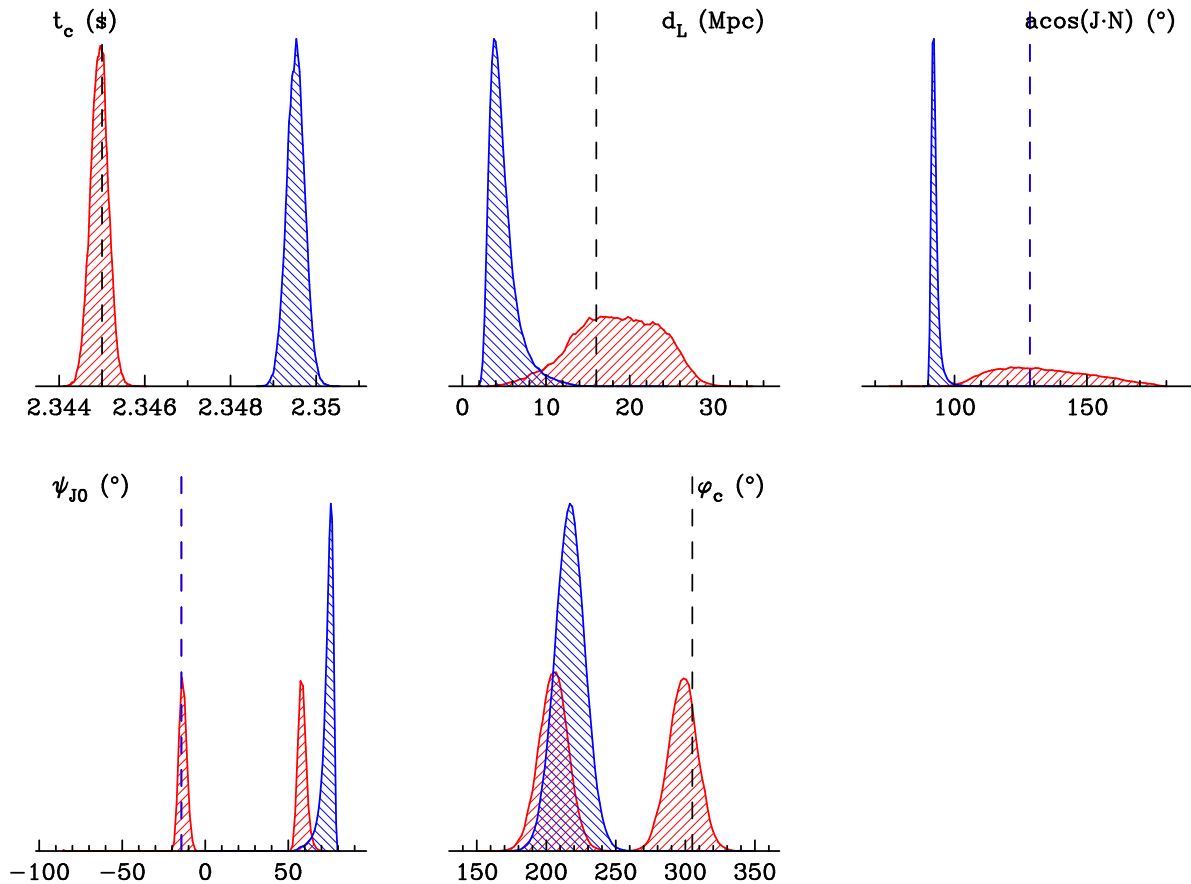
Figure 3. One-dimensional PDFs for the runs of experiment 2a (red, hatched upward) and of the runs in experiment 2b (blue, hatched downward), in the non-spinning case. The black dashed lines mark the values of the injected parameters. The level of support is indeed smaller in the second case.

wave signal we injected *and* have its sky location in the gap. And by giving preference to more likely solutions the parameter estimation routine is in fact doing the right, completely reasonable thing. The PDFs of the relevant parameters for the comparison of experiments 1 and 3 are plotted in figure 4. The PDFs in the other parameters are also very similar in both the original run and the third experiment run.

When the BH is spinning moderately, the two signals injected in experiment 1 and in experiment 3 are different (as we can infer from the large difference in likelihood in experiment 2b, and the smaller match, see table 2). The different injections yield significantly different PDFs for the sky position (figure 2b) as well as for the other parameters, as we checked in our study.

4.3. Comparison of MCMC runs with 1.5-pN and 3.5-pN waveforms

So far we have used 1.5-pN waveforms for computational efficiency. However, in this section we used our MCMC implementation to present the first comparison of the accuracy of parameter estimation with the 1.5-pN and 3.5-pN waveform families, as described in section 2. In both cases, we injected BH-NS binary inspiral waveforms
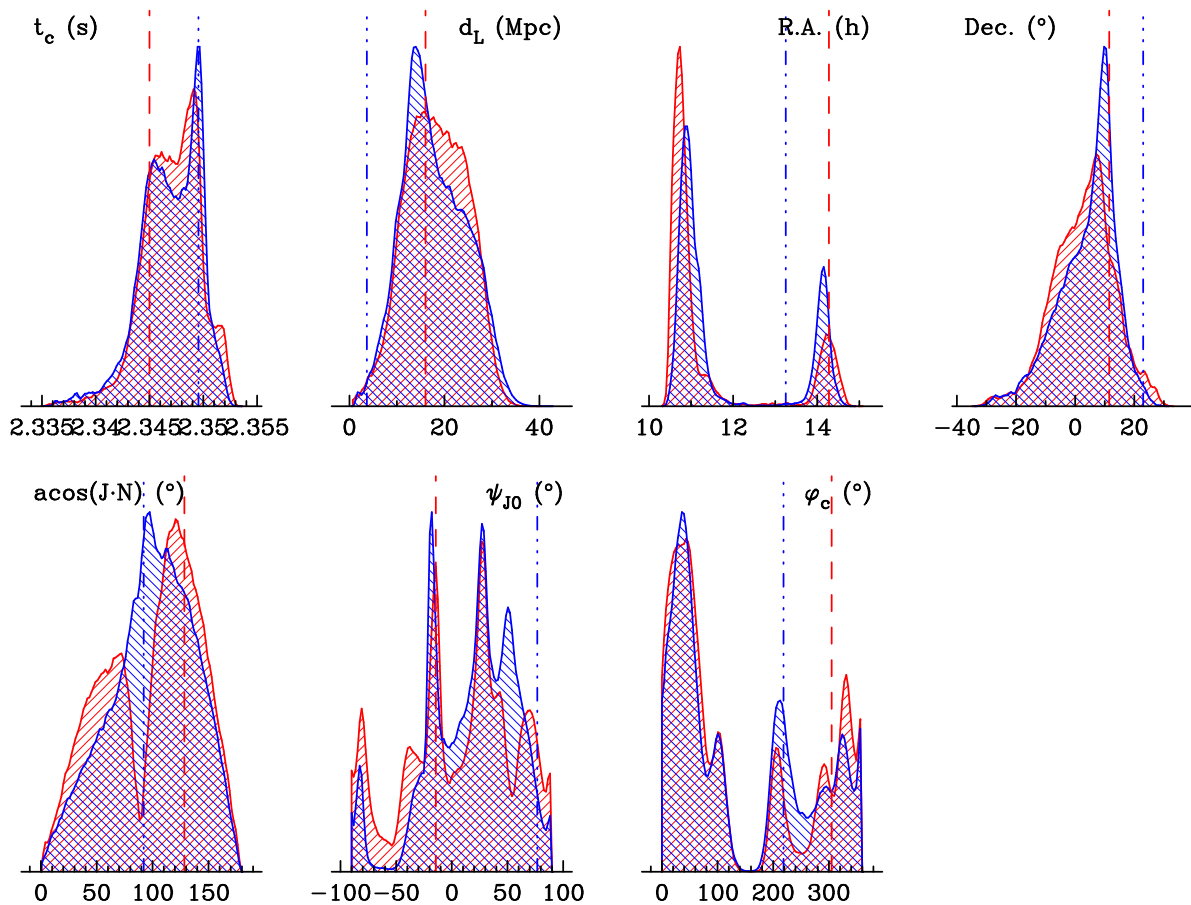
Figure 4. One-dimensional PDFs for the reference run in experiment 1 (red, hatched from bottom-left to top-right) and of the runs in experiment 3 (blue, hatched from top-left to bottom-right), in the non-spinning case. The dashed lines mark the values of the injected parameters in experiment 1, while the dotted-dashed lines mark the values of the injected parameters in experiment 3. The PDFs for all parameters are very similar for the two injections.

with a non-spinning BH into the noise of a single interferometer (H1). We analyzed the 1.5-pN injected waveform with an MCMC with 1.5-pN waveform templates, and the 3.5-pN injected waveform with 3.5-pN waveform templates. We scaled the distance to the source to obtain a signal to noise ratio of 20.0 in both cases, which resulted in a distance of ~ 11.9 Mpc for the 1.5-pN waveform case, and ~ 12.2 Mpc for the 3.5-pN waveform case. The remaining injection parameters were set to $a_{\rm spin} = 0.0$, $\mathcal{M} = 3.0 M_\odot$, $\eta = 0.11$ ($M_1 = 10.0 M_\odot$, $M_2 = 1.4 M_\odot$), R.A. $= 17.3$ h, Dec $= -5°$, $\theta_{J_0} = -23°$, $\phi_{J_0} = 194°$, $\phi_{\rm c} = 352°$ and $t_{\rm c} = 894377000.500244$ s for this study. The three spin parameters ($a_{\rm spin}$, θ_{SL} and $\alpha_{\rm c}$) were fixed, forcing the chains to explore a parameter space that was effectively 9-dimensional.

Figure 5 compares the probability-density functions (PDFs) of the mass parameters for the runs with the 1.5-pN and 3.5-pN waveforms for $1.5 * 10^6$ iterations in both cases. It is evident that the estimation of the symmetric mass ratio η is more accurate in the 3.5-pN case, which results in better constraints on the individual masses. The 2-σ

probability ranges for the chirp mass are roughly similar in both cases (a factor of 1.2 narrower when the 3.5-pN waveform is used), whereas for η, and hence for the individual masses, the ranges are narrower by a factor of 1.8 when the 3.5-pN waveform is used. The additional information in the higher-order pN waveforms results in a greater structure of the parameter space. In principle this extra structure allows us to estimate the binary parameters more accurately. However, a more structured parameter space also affects the sampling efficiency of our MCMC code negatively, so that we need more iterations to obtain a well-sampled MCMC run. In addition, the computation of a single 3.5-pN waveform template takes about 2.4 times longer than that of a 1.5-pN template. This effect prevents us, for now, from performing this analysis in a full 12-dimensional or 15-dimensional parameter space in a reasonably short computational time.

One of the ways to speed up the convergence of the code is to use faster, lower-order pN waveform templates during the *burn-in* phase and to use the additional information provided by the more expensive, higher-order pN waveforms to sample the true mode of the PDF accurately. In addition, we have plans to use time annealing (Gair et al. 2008), starting the MCMC runs on only a fraction of the available time-domain data, so that only a part of the waveform template needs to be computed for each iteration. These improvements will speed up the computation of each waveform template and the loss of information will allow the Markov chains to move through parameter space more easily until they lock on to the true modes of the PDF. If the amount of information is then gradually increased (by increasing the pN order of the waveforms or the time duration of the data set), the accuracy of parameter estimation will be improved.

5. Conclusions

We have explored the degeneracies in the sky position for a gravitational-wave observation of an inspiral of a BH-NS binary with two non-colocated ground-based interferometers. Whereas simple triangulation based on time delays alone would result in a homogeneous sky ring, our MCMC runs show (in experiment 1) an incomplete ring in the sky consisting of arcs separated by gaps. While the arcs make up most of the circumference of the sky ring for an inspiral with a non-spinning BH, these arcs become smaller when spin is present and may be reduced to a single arc for the case of moderate spin and a sufficient misalignment between the BH spin and the orbital angular momentum. We demonstrated that in the spinning case, the maximum likelihood values are in fact lower in the gaps than in the arcs. In the non-spinning case the likelihood in the gaps can actually be as high as in the arcs; however the gaps can be explained by a smaller volume of support in the other extrinsic parameters, such as the binary orientation and distance (experiment 2). It is then less likely for the chains to sample this smaller volume in parameter space, resulting in gaps in the two-dimensional sky probability density function. In the non-spinning case, if a source is located in a gap, the posterior PDF still has a gap at the true source sky location (experiment 3).

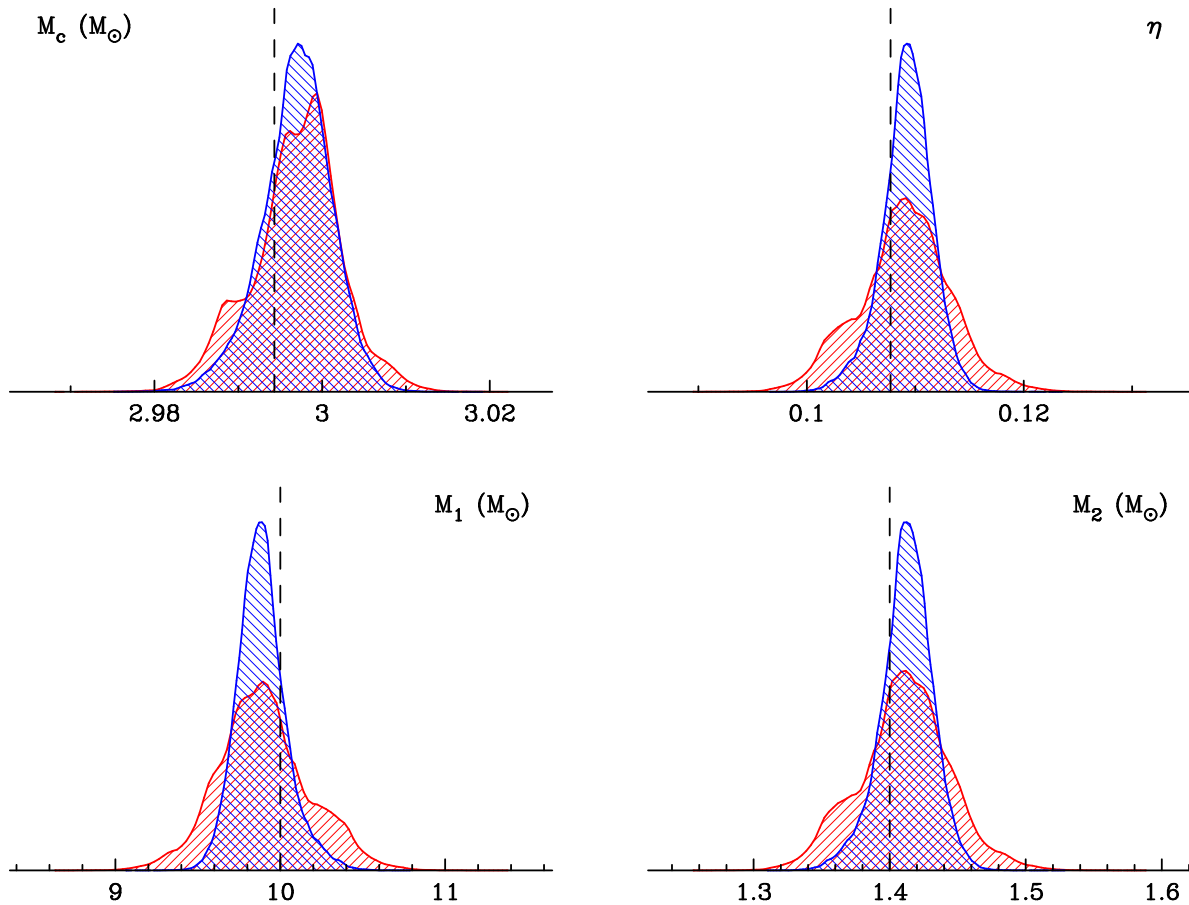The subject of estimating the position of a gravitational-wave source on the sky

Figure 5. PDFs from a run with chains starting from the true values, with the 1.5-pN waveform (red, hatched from bottom-left to top-right) and the 3.5-pN waveform (blue, hatched from top-left to bottom-right) from a non spinning source. Only one detector (LIGO at Hanford) is used.

has been explored by many researchers, in the context of binary-inspiral and burst signals; the assumed baseline for these studies corresponds to three detectors located at the three LIGO-Virgo observatory positions, and operating at their design sensitivities. For detectable burst sources (SNR>5), arrival-time techniques should allow a precision of about 1° for the source direction (Cavalier et al. 2006). A method that takes into account burst-signal arrival time and amplitude, plus arrival-time uncertainties equivalent to what is observed with real LIGO and Virgo data, gives source uncertainties of a few degrees (Markowitz et al. 2008). Coherent techniques also exist for burst detection and sky-location determination, but by their own admission these methods are computationally costly (Searle et al. 2008). Many techniques have also been developed for sky localization for binary-inspiral events. It has been shown, using time and mass parameter estimates, that the LIGO-Virgo network could localize the position of a binary-neutron-star inspiral to an accuracy of 4° if it were located in M87 (16 Mpc), or 2° for a source in NGC 6744 (10 Mpc) (Beauville et al. 2008); coherent methods, which also depend on estimating the time and mass parameters, give similar accuracies (Ajith

& Bose 2009).

MCMC parameter-estimation methods, like those used in this study, are capable of estimating the sky parameters, along with all of the other signal parameters; this is one reason why MCMC methods are computationally intensive. Coherent MCMC methods applied to signals observed by the LIGO-Virgo network will be able to resolve the sky location to 2° for signals with an SNR of 15 (Röver et al. 2007b). When the compact objects have spin, and the search templates account for this parameter, sky localization becomes relatively more accurate for higher values of spin (van der Sluys et al. 2008b). It is important to remember that, in principle, the MCMC results show the best constraints one could hope to place on signal parameters (including the sky location) by displaying the true posterior PDFs. While comparisons with other particular sky-localization results may be cumbersome because different waveforms were assumed at different SNRs in different detectors, MCMC produced posterior PDFs display the statistically correct and most precise localization. Bayesian methods achieve better parameter-estimation accuracy when the template model describes the functional form of the actual signal more accurately. When a gravitational-wave detection occurs, it is likely that all possible sky localization algorithms will be used, and the methods should be considered to be complementary.

In section 4.3, we compared MCMC results on software injections using waveform families of 1.5-pN and 3.5-pN order for both the injections and the MCMC parameter estimation. We have shown that the higher-order templates have the potential for more accurate parameter estimation, but that sampling the parameter space with these templates is more computationally difficult. However, a number of upcoming improvements should improve the sampling efficiency of our MCMC runs.

The analysis presented here is the second step of a more detailed study that we are currently carrying out, exploring a much larger parameter space, developing techniques to reduce the computational cost of these simulations, and testing the methods with actual LIGO data. We are in the process of updating our MCMC code to include the spin of the second binary member, increasing the dimensionality of the parameter space from 12 to 15. Finally, we intend to further develop our Bayesian approach into a standard tool that can be included in the follow-up analysis pipeline used for the processing of the 'science data' collected by ground-based laser interferometers.

Acknowledgments

References

Acernese F, Amico P & al. 2004 *Class. Quant. Grav.* **21**(5), S385–S394.

Ajith P & Bose S 2009 *arXiv: gr-qc/0901.4936* .

Apostolatos T A, Cutler C, Sussman G J & Thorne K S 1994 *Phys. Rev. D* **49**, 6274–6297.

Atchadé Y F & Rosenthal J S 2005 *Bernoulli* **11**(5), 815–828.

Barish B C & Weiss R 1999 *Physics Today* **52**, 44–50.

Beauville F, Bizouard M A, Blackburn L, Bosi L, Brocco L, Brown D A, Buskulic D, Cavalier F, Chatterji S, Christensen N, Clapson A C, Fairhurst S, Grosjean D, Guidi G, Hello P, Heng S, Hewitson M, Katsavounidis E, Klimenko S, Knight M, Lazzarini A, Leroy N, Marion F, Markowitz J, Melachrinos C, Mours B, Ricci F, Viceré A, Yakushin I, Zanolin M & The joint LIGO/Virgo working group 2008 *Class. Quant. Grav.* **25**(4), 045001–+.

Blanchet L, Buonanno A & Faye G 2006 *Phys. Rev. D* **74**(10), 104034.

Buonanno A, Chen Y & Vallisneri M 2003 *Phys. Rev. D* **67**(10), 104025.

Cavalier F, Barsuglia M, Bizouard M A, Brisson V, Clapson A C, Davier M, Hello P, Kreckelbergh S, Leroy N & Varvella M 2006 *Phys. Rev. D* **74**(8), 082004–+.

Cutler C & Thorne K S 2002 *Proceedings of GR16, World Scientific, Singapore* .

Faye G, Blanchet L & Buonanno A 2006 *Phys. Rev. D* **74**(10), 104033.

Figueiredo M A T & Jain A K 2002 *IEEE Transactions on pattern analysis and machine intelligence* **24**(3), 381–396.

Fritschel P 2003 *in* M Cruise & P Saulson, eds, 'Society of Photo-Optical Instrumentation Engineers (SPIE) Conference Series' Vol. 4856 of *Presented at the Society of Photo-Optical Instrumentation Engineers (SPIE) Conference* pp. 282–291.

Gair J R, Porter E, Babak S & Barack L 2008 *Class. Quant. Grav.* **25**(18), 184030–+.

Gelman A, Carlin J B, Stern H & Rubin D B 1997 *Bayesian data analysis* Chapman & Hall, Boca Raton.

Gilks W R, Richardson S & Spiegelhalter D J 1996 *Markov chain Monte Carlo in practice* Chapman & Hall/CRC.

Grandclément P, Kalogera V & Vecchio A 2003 *Phys. Rev. D* **67**(4), 042003.

Kidder L E 1995 *Phys. Rev. D* **52**, 821–847.

Lang R N & Hughes S A 2006 *Phys. Rev. D* **74**(12), 122001.

LIGO Scientific Collaboration 2007 The LSC Algorithm Library. https://www.lsc-group.phys.uwm.edu/daswg/projects/lal.html.

Markowitz J, Zanolin M, Cadonati L & Katsavounidis E 2008 *Phys. Rev. D* **78**(12), 122003–+.

O'Shaughnessy R, Kim C, Kalogera V & Belczynski K 2008 *ApJ* **672**, 479–488.

Röver C, Meyer R & Christensen N 2006 *Class. Quant. Grav.* **23**, 4895–4906.

Röver C, Meyer R & Christensen N 2007a *Phys. Rev. D* **75**(6), 062004.

Röver C, Meyer R, Guidi G M, Viceré A & Christensen N 2007b *Class. Quant. Grav.* **24**, 607–+.

Searle A C, Sutton P J & Tinto M 2008 *arXiv: gr-qc/0809.2809* .

Stroeer A, Veitch J, Röver C & al. 2007 *Class. Quant. Grav.* **24**, 541.

van der Sluys M, Raymond V, Mandel I, Röver C, Christensen N, Kalogera V, Meyer R & Vecchio A 2008a *Class. Quant. Grav.* **25**(18), 184011–+.

van der Sluys M V, Röver C, Stroeer A, Raymond V, Mandel I, Christensen N, Kalogera V, Meyer R & Vecchio A 2008b *ApJ* **688**, L61–L64.

Vecchio A 2004 *Phys. Rev. D* **70**(4), 042001.

Will C M & Wiseman A G 1996 *Phys. Rev. D* **54**, 4813–4848.

Willke B, Aufmuth P & al. 2004 *Class. Quant. Grav.* **21**, 417.